Matter

CellPress
OPEN ACCESS

Article

Post-synthesis tuning of dielectric constant via ferroelectric domain wall engineering

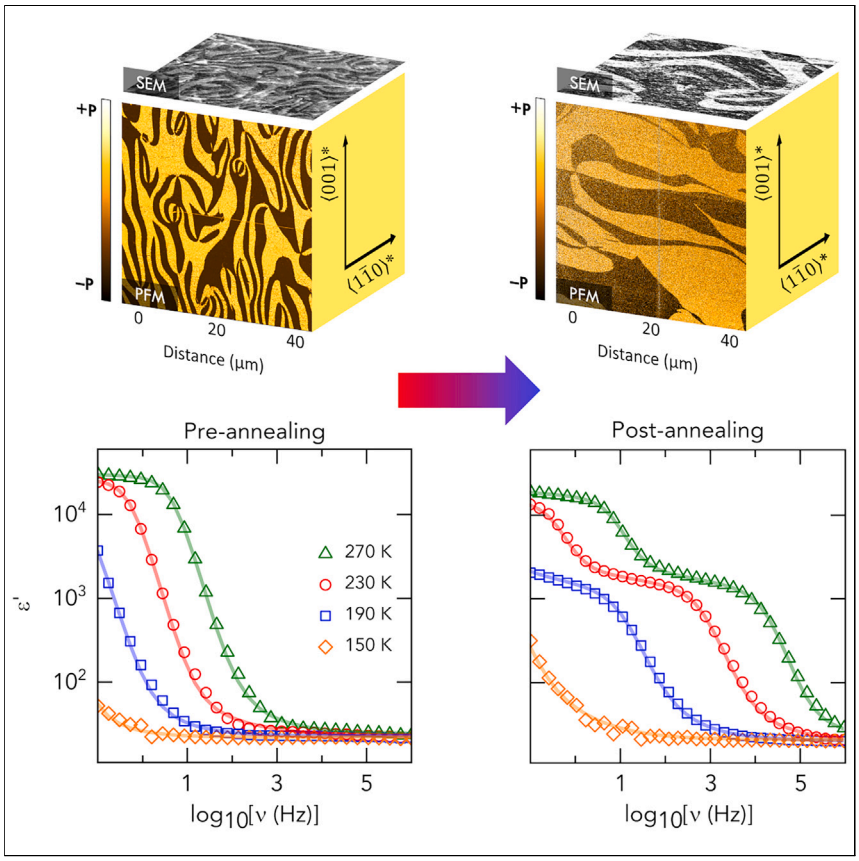

Materials with high dielectric constants are essential for electronic technology, with the values of the dielectric constant typically established during synthesis. Utilizing improper ferroelectric hexagonal $ErMnO_3$ as a template material, Zhou et al. demonstrate that the dielectric constant of a material can be tuned post-synthesis by adjusting the number of insulating domain walls. Furthermore, they show that these insulating domain walls exhibit ideal capacitor behavior, enabling the authors to predict the optimal configuration for maximizing a material's dielectric constant with insulating domain walls.

Lima Zhou, Lukas Puntigam, Peter Lunkenheimer, ..., Stephan Krohns, Jan Schultheiß, Donald M. Evans

donald.evans@warwick.ac.uk

Highlights

Insulating domain walls can be treated as ideal capacitors

Dielectric constants can be tuned *in situ* by changing the number of domains

Dielectric constant is maximized for a material with one insulating domain wall

2 Benchmark
First qualification/assessment of material properties and/or performance

Zhou et al., Matter 7, 2996–3006
September 4, 2024
Published by Elsevier Inc.
https://doi.org/10.1016/j.matt.2024.04.024

CellPress
OPEN ACCESS

Matter

Article

Post-synthesis tuning of dielectric constant via ferroelectric domain wall engineering

Lima Zhou,[1] Lukas Puntigam,[1] Peter Lunkenheimer,[1] Edith Bourret,[2] Zewu Yan,[2,3] István Kézsmárki,[1] Dennis Meier,[4] Stephan Krohns,[1] Jan Schultheiß,[4] and Donald M. Evans[1,5,6,*]

SUMMARY

A promising mechanism for achieving colossal dielectric constants involves the use of insulating internal barrier layers, such as insulating domain walls in ferroelectrics. A key advantage of domain walls, compared to other stationary interfaces, is their mobility, offering the potential for post-synthesis adjustment of the dielectric constant. In this work, we demonstrate that altering the domain wall density enables the tuning of the dielectric constant in our template material, i.e., hexagonal $ErMnO_3$ single crystals. Through microscopy and macroscopic dielectric spectroscopy, we quantify changes in domain wall density and correlated these with changes in dielectric constant within a single sample. Analysis of the dielectric data suggests that the insulating domain walls act as "ideal" capacitors connected in series. Our approach to engineering the domain wall density can be readily extended to other control methods, e.g., electric fields or mechanical stresses, providing a degree of flexibility to *in situ* tune the dielectric constant.

INTRODUCTION

Materials with high dielectric constants are of considerable importance for applications, playing a key role in, e.g., short-term energy storage in capacitors,[1–3] and they ensure the performance of today's smartphones, portable computers, and electric vehicles. For this, a high dielectric constant and low loss tangent are important criteria.[4] Materials with very high dielectric permittivity ($\varepsilon' > 1{,}000$) are often referred to as having "colossal dielectric constants" (CDCs),[5,6] offering performance parameters of great technological interest. There are two typical approaches to achieve such colossal values: (1) choose a material that naturally exhibits such traits using, e.g., the CDC that arises across a ferroelectric transition[7] or (2) engineer insulating layers within a material to act as barrier layer capacitors (BLCs).[5,8] What both of these approaches have in common is that colossal values are achieved during material synthesis and then "locked in" to the material. An example of approach (1) is $Pb(Zr_x,Ti_{1-x})O_3$ (PZT), which displays both a CDC and a low-loss tangent.[9] The room temperature dielectric constant of PZT can exceed 10^3 with a loss tangent of $\tan\delta < 10^{-2}$. A common example of (2) is the BLCs observed in ceramics, where they form at insulating grain boundaries and at metal-semiconductor interfaces due to the formation of a Schottky barrier.[5,6,10,11] Such barrier layers are associated with a step-like increase in ε' and a peak in ε'', representing a "Debye-like," so-called Maxwell-Wagner (MW) relaxation process.[5,12–14] For a more detailed discussion, the interested reader is referred to, for example, the review of Lunkenheimer et al.[5]

The concept of using internal barrier layers at grain boundaries[8,12] has recently been expanded toward ferroelectric domain walls (DWs).[15,16] Such DWs naturally arise as

PROGRESS AND POTENTIAL

Materials with high dielectric constants are crucial for many modern electrical devices. Several approaches are used to achieve these high dielectric constants, typically during the growth process. In this study, Zhou et al. demonstrate that by using insulating domain walls as nanoscale capacitors, they can alter the dielectric constant of a material after synthesis by adjusting the number of domain walls. Furthermore, Zhou et al. model their observations to show that in hexagonal $ErMnO_3$, the domain walls behave as ideal capacitors and provide an equation to predict the effective dielectric constant. Excitingly, this equation implies that there is no hard theoretical maximum to the achievable dielectric constant for a sample with a single domain wall, with the practically realizable value depending on the sample size. These findings hold promise for the development of next-generation dielectric materials.

a result of the formation of spontaneous polarization domains, and their density can readily be engineered via, e.g., electric fields, mechanical pressure, microstructural levers, or annealing, which gives additional opportunities for tailoring dielectric properties.[17] Particularly intriguing in this context are improper ferroelectrics, where the polarization is not the primary symmetry-breaking order parameter. It has been discovered that these systems can develop stable insulating DWs[18,19] that can act as BLCs.[15,16] Further, the DWs in improper ferroelectrics are particularly stable to electric fields, compared to proper ferroelectrics, because the electric field is not the conjugate field to the primary order parameter.[20,21] To date, however, the concept has only been explored at a proof-of-concept level,[15,16] whereas direct imaging of the DW density together with a corresponding quantitative derivation of the changes in the macroscopic dielectric constant in a single sample is missing.

The family of hexagonal manganites has a room temperature $P6_3cm$ symmetry arising from a high-temperature phase with $P6_3/mmc$ symmetry.[22] It was among the first material families to show stable charged DWs with unusual electronic properties.[18,23,24] In this work, we choose single-crystalline hexagonal $ErMnO_3$ as a template material, as it is a well-studied improper ferroelectric ($P \approx 5.5\ \mu C/cm^2$ and Curie temperature [T_C] $\approx$ 1,150°C) with stable charged DWs.[22,25,26] We show that post-synthesis engineering of the DW density in $ErMnO_3$ changes the material's dielectric constant. We quantify the DW density and variations in the dielectric constant by applying different microscopy techniques, as well as dielectric measurements recorded before and after thermal annealing. We observe a direct correlation between changes in the density of (insulating) DWs and the macroscopic dielectric response, establishing DW engineering as a powerful tool for achieving tunable dielectric constants and CDCs post-synthesis.

RESULTS

Control of microstructure

The $ErMnO_3$ crystal used in this study is cut from the same single crystal used by Puntigam et al.[15] and was grown by the pressurized floating zone method.[27] The sample was measured as prepared and after subjecting it to thermal treatment as indicated in Figure 1A. To quantify the DW density in our $ErMnO_3$ crystal, we image the ferroelectric domain structure using piezoresponse force microscopy (PFM) and scanning electron microscopy (SEM). The initial domain structure is presented in Figure 1B. The gold-brown side panel of Figure 1B shows the in-plane piezoresponse of $ErMnO_3$, revealing the characteristic domain pattern with 6-fold vertices as explained elsewhere.[22,28,29] Note that in this work, we interpret the word "vortex" to represent a continuous rotation, e.g., the continuous rotation of the structural order parameter in the hexagonal manganites, while we use the word "vertex" for the meeting point of multiple objects, e.g., the 6-fold meeting point of different ferroelectric domains in the hexagonal manganites. Because this work focuses on the polarization properties, we use the word vertex to refer to these meeting points. The PFM measurement is complemented by the top SEM image (black and white) of the polar surface, corroborating the formation of an isotropic domain structure (for details concerning SEM contrast formation in hexagonal manganites, see, e.g., Roede et al.[30] and Hunnestad et al.[31]). Based on the imaging experiments, the vertex density can be estimated by counting the number of vertexes present and dividing that value by the area of the image. This gives a vertex density of approximately 0.0125 vertices/μm^2 in the as-grown state.

By applying the thermal treatment illustrated in Figure 1A, the vertex density in $ErMnO_3$ can be controlled,[22,32,33] providing a viable handle for a reduction of the

[1]Experimental Physics V, Center for Electronic Correlations and Magnetism, University of Augsburg, 86159 Augsburg, Germany

[2]Materials Sciences Division, Lawrence Berkeley National Laboratory, Berkeley, CA 94720, USA

[3]Department of Physics, ETH Zurich, 8093 Zurich, Switzerland

[4]Department of Materials Science and Engineering, Norwegian University of Science and Technology (NTNU), 7043 Trondheim, Norway

[5]Department of Physics, University of Warwick, Coventry CV4 7AL, UK

[6]Lead contact

*Correspondence: donald.evans@warwick.ac.uk

https://doi.org/10.1016/j.matt.2024.04.024

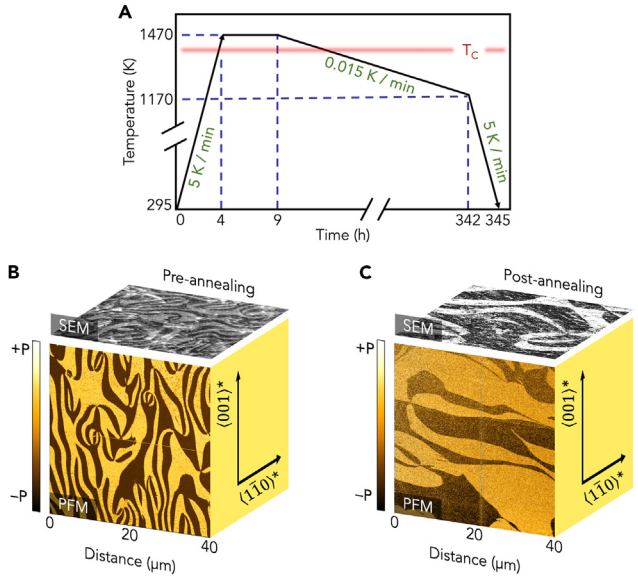

Figure 1. Ferroelectric domain structure in $ErMnO_3$ before and after thermal treatment

(A) Protocol used for the thermal treatment where T_C is represented by the red line.

(B) The ferroelectric domain structure before thermal treatment.

(C) The ferroelectric domain structure after thermal treatment.

Both (B) and (C) show representative PFM images of the non-polar surface (yellow and brown) and SEM images of the domain structure of the polar surface (black and white).

number of DWs in the system. This is confirmed by the PFM and SEM images in Figure 1C, which are recorded after thermal annealing (with a cooling rate of 0.015 K/min) through the transition region around the T_C.[32] We note that after annealing, the sample was re-polished to ensure a flat surface for the PFM and SEM imaging of bulk properties following the procedure outlined in Puntigam et al.[15] Both the SEM and PFM images reveal a significantly reduced density of vertices, i.e., around 0.0025 vertices/μm^2, and consequently an increased domain size. As each vertex should connect six DWs, this observation shows that the number of DWs, including the insulating (head-to-head) DWs,[18] is reduced by nearly an order of magnitude.

Dielectric properties

After demonstrating that the vertex density, and hence the DW density, is reduced by the applied thermal annealing procedure, consistent with the literature,[32] we next turn to the bulk dielectric properties. The real part of the dielectric constant, ε', and the loss tangent, tan δ, are recorded for the pre-annealing state, i.e., for the domain state seen in Figure 1B, and are given in Figures 2A and 2B, respectively. $\varepsilon'(T)$ exhibits a rapid increase with increasing temperature before plateauing. This increase shifts to higher temperature for higher frequencies, moving outside our measurement range for frequencies above ~12 kHz. After thermal treatment (leading to the domain state in Figure 1C), marked differences in both the real part and tan δ were observed, as shown in Figures 2C and 2D, respectively. Notably, the rapid increase now occurs approximately 50 K lower in temperature, and a second step-like increase is now evident, as seen, e.g., in the 1 Hz dataset of Figure 2C.

Additionally, Figures 2B and 2D reveal that the step-like increases correspond to peaks in tan δ, indicating that they originate from relaxation processes.

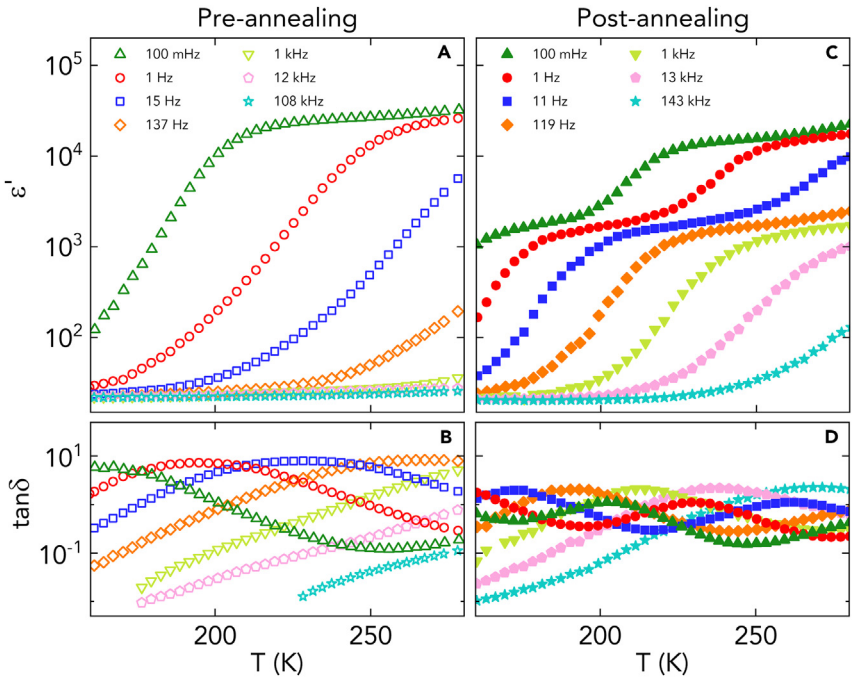

Figure 2. Effect of changing DW density on the dielectric response

(A) The real part of the dielectric constant at representative frequencies as a function of temperature of the pre-annealed sample.

(B) The loss tangent for representative frequencies of temperature for the pre-annealed sample.

(C) The real part of the dielectric constant at representative frequencies as a function of temperature of the post-annealed sample.

(D) The loss tangent for representative frequencies of temperature for the post-annealed sample.

Relaxation-like features, as in Figures 2A–2D, are common in oxide materials and often originate from internal BLCs (IBLCs) and/or surface BLCs (SBLCs).[5,6] IBLCs arise from MW polarization effects at interfaces within the material, such as DWs, whereas SBLCs often result from the formation of Schottky barriers at the sample-electrode interfaces and the associated depletion zone acting as a thin insulating layer.[5,6]

For a more detailed analysis of the change in dielectric properties, in Figure 3, we present the spectra at four representative temperatures. Figure 3A shows the frequency-dependent ε' values for 150, 190, 230, and 270 K. In addition, Figure 3B provides frequency-dependent conductivity data, $\sigma'(\nu)$, at the same temperatures. Using the 270 K data displayed in Figure 3A as representative examples, at high frequencies ($\nu \geq 10^3$ Hz), ε' flattens out to a nearly constant value, consistent with data reported in the literature.[15,16] At lower frequencies ($\nu \lesssim 10^3$ Hz), there is a relaxation-like feature in ε', leading to a step-like increase by about three decades to colossal values of ε' on the order of 10^4.

Figures 3C and 3D show ε' and σ' measured after thermal treatment, i.e., for the sample with a reduced number of DWs. As before, we use the 270 K data of Figure 3C as representative examples of the post-annealing properties. While the dielectric constant approached at high frequencies is the same as for the untreated sample, at lower frequencies, there are now two distinct relaxations instead of the single process observed pre-annealing (Figure 3A). For instance, at 270 K in Figure 3C, there is a step-like increase in ε' from ~21 to ~2,500 for 10^3 Hz $\lesssim \nu \lesssim 10^5$ Hz, followed by a second step-like increase in ε' from ~2,500 to ~2×10^4 for

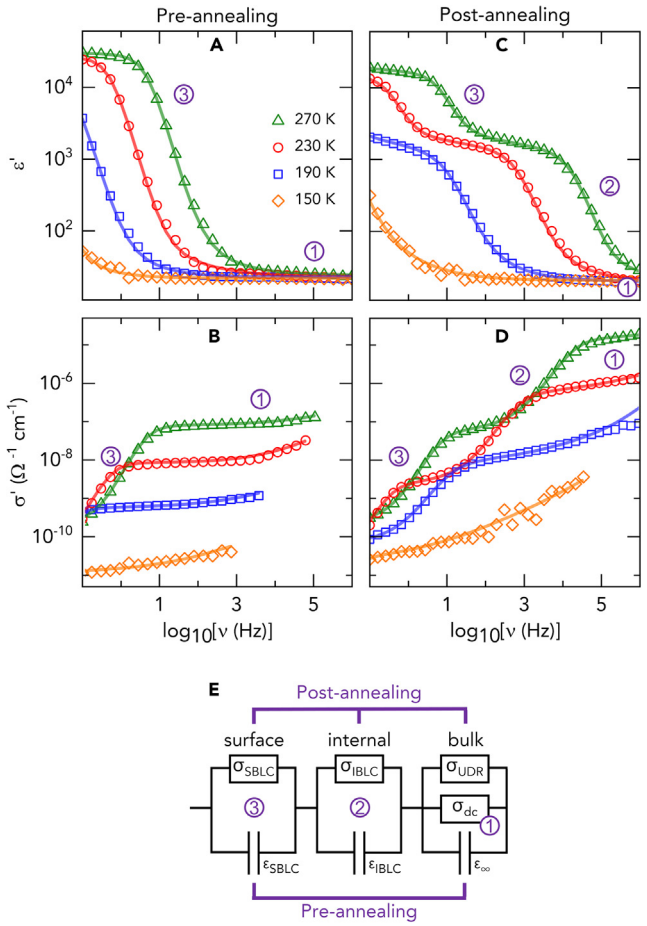

Figure 3. DW density correlations with the dielectric properties

(A) Frequency-dependent dielectric permittivity pre-annealing.

(B) Frequency-dependent conductivity data pre-annealing.

(C) Frequency-dependent dielectric permittivity post-annealing.

(D) Frequency-dependent conductivity data post-annealing.

(E) Equivalent circuit model used to fit the data.

In all plots, fits are given by solid lines, with fit parameters provided in Table 1. In all plots, the green triangles collected at 270 K, the red circles at 230 K, the blue squares at 190 K, and the orange diamonds at 150 K. Numbers "1," "2," and "3" indicate the contribution of specific RC-circuit elements in the dielectric spectra.

$\nu \lesssim 100$ Hz. A similar succession of relaxation features is also observed in the conductivity data in Figure 3D. Here, one should note that the dielectric loss ε'' is related to σ' via $\varepsilon'' \propto \sigma'/\nu$. Thus, the observed steps in $\sigma'(\nu)$ (Figures 3B and 3D) correspond to peaks in $\varepsilon''(\nu)$, shifting with temperature, which is the typical signature of a relaxation process. Before thermal treatment (Figure 3B), the 270 K curve shows a single plateau between ~10 and ~10^5 Hz at $\sigma' \approx 8 \times 10^{-8}$ $(\Omega\text{cm})^{-1}$ and a step-like decrease for $\nu \lesssim 1$ Hz. After thermal treatment (Figure 3C), two plateaus are observed with a value of $\sigma' \approx 1.5 \times 10^{-5}$ $(\Omega\text{cm})^{-1}$ at frequency, (ν), $\geq 10^5$ Hz. Both before and after treatment, we observe an increase of $\sigma'(\nu)$, superimposed to the high-frequency plateaus, which can be ascribed to a so-called "universal dielectric response" (UDR), where σ' follows a power-law behavior.[34] It is commonly ascribed to hopping charge transport[5,35] and is most clearly revealed at 150 K, in the post-annealing state (Figure 3D), where the relaxation-related step has shifted out of the frequency window. Notably, other studies on the closely related hexagonal manganite $YMnO_3$ showed

Table 1. Fitting parameters for ε' and σ' used in the equivalence circuit model

	T (K)	ε_∞ ①	ε' ②	ε' ③	σ_{dc}^{bulk} $(\Omega cm)^{-1}$ ①	σ_{dc}^{IBLC} $(\Omega cm)^{-1}$ ②	σ_{dc}^{SBLC} $(\Omega cm)^{-1}$ ③
Pre-annealing	270	24	–	31,000	7.6×10^{-8}	–	2.1×10^{-10}
Pre-annealing	230	23	–	28,000	8.1×10^{-9}	–	5.3×10^{-11}
Pre-annealing	190	22	–	31,000	5.4×10^{-10}	–	8.4×10^{-12}
Post-annealing	270	21	2,500	20,000	1.6×10^{-5}	8.0×10^{-8}	2.3×10^{-10}
Post-annealing	230	21	2,500	20,000	5.7×10^{-7}	3.6×10^{-9}	2.7×10^{-12}
Post-annealing	190	21	2,500	20,000	8.7×10^{-9}	9.2×10^{-11}	3.4×10^{-14}

All values are rounded to 2 significant figures.

qualitatively similar behavior,[16] including the occurrence of two well-resolved MW relaxations with a reduced DW density (0.04 vertices/μm^2), whereas only a single clear relaxation step was observed in a different $YMnO_3$ sample with 1.5 vertices/μm^2. The key observation from Figure 3 is that the density of DWs correlates with the dielectric properties of the same sample and, hence, can be used to tune them. We note that this is a physically different method of tuning dielectric constants compared to conventional heat treatment methods that are based on modifications to stoichiometry.

Dielectric analysis

In order to disentangle the different contributions to the dielectric response, we use an equivalent circuit analysis to fit the frequency-dependent data. Following the established procedure in literature,[5,6,16] individual parallel RC elements, connected in series to each other, are used to represent the different contributions: the SBLC, the IBLC, and the bulk. This is pictorially represented in Figure 3E. The RC element for the bulk has an additional frequency-dependent impedance connected in parallel to represent the contribution of the UDR. A detailed description of this approach is provided in Lunkenheimer et al.,[5] and examples of its implementation in this material class can be found in Puntigam et al.,[15] Ruff et al.,[16] and Holstad et al.[36] The fits are shown by the solid lines in Figures 3A–3D and provide a reasonable description of the experimental data. The corresponding fitting parameters are given in Table 1. The high-frequency plateau in $\sigma'(\nu)$ (denoted "1" in Figures 3B and 3D) and the superimposed UDR represent the bulk response, as here the interface contributions are shorted by their respective capacitances.[5,6] Correspondingly, at higher frequencies, $\varepsilon'(\nu)$ approaches its intrinsic value, which is of the order of 20 (Figures 3A and 3C). In accordance with previous investigations of this and related materials,[15,16] the high-frequency step in the post-annealing state (denoted "2") is attributed to IBLCs originating from insulating DWs, which leads to an MW relaxation. The second step at lower frequencies ("3") is ascribed to an MW relaxation caused by SBLCs, e.g., arising from the metal-semiconductor contacts.[5,15,16] While in the pre-annealing state there is only a single interface-related RC circuit required to reproduce the experimental findings (denoted "3" in Figure 3B), the IBLC relaxation step is expected to still be present but superimposed with the MW relaxations from SBLC. This changes after annealing: comparing the high-frequency plateaus of $\sigma'(\nu)$ in Figures 3B and 3D reveals that the bulk conductivity strongly increases upon thermal treatment, potentially due to a change in the stoichiometry, or the defect structure, of the material.[37–40] As the MW relaxation time is proportional to the bulk resistivity,[5,6] this moves the IBLC relaxation step to higher frequencies, allowing it to be distinguished from the dominating SBLC relaxation.

Having experimentally established that changes in DW density impact the dielectric spectra, next, we aim to quantitatively estimate the influence of the DW density on the value of the CDCs related to the MW relaxation process caused by IBLCs. To find

this correlation, we make two reasonable assumptions[16]: (1) the interface resistance (the IBLC resistance in the present case) is much higher than the bulk resistance, i.e., we have insulating interfaces acting as capacitors, and (2) the overall interface thickness is much smaller than the bulk thickness, i.e., in Figure 3E, the IBLC capacitance is much larger than the bulk capacitance. Compared to the intrinsic bulk dielectric constant, ε_b, the colossal plateau of ε' of an interface-generated MW relaxation, ε_{col}, is then generally enhanced by a factor that is given by the thickness ratio of the bulk and the interface.[16,41] This arises from the fact that the apparently colossal ε_{col} is calculated using the bulk thickness instead of the several decades smaller interface thickness, the latter leading to large capacitance. When assuming that the intrinsic dielectric constant of the interface, ε_i, is the same as for the bulk, i.e., $\varepsilon_i = \varepsilon_b$, this leads to

$$\varepsilon_{col} = \varepsilon_b \frac{d_b}{d_i}, \qquad \text{(Equation 1)}$$

where d_b and d_i are the thicknesses of the bulk sample and the interface, respectively. In the present case, ε_b is given by ε_∞ of the MW relaxation, read off at high frequencies and low temperatures in Figures 3A and 3C, where the interface-related RC circuits are effectively short circuited, and the intrinsic response is detected. Then, the above assumption $\varepsilon_i = \varepsilon_b$ (which, in our case, corresponds to $\varepsilon_{IBLC} = \varepsilon_\infty$, where ε_{IBLC} is the intrinsic dielectric constant in the DWs) should be approximately fulfilled: it is reasonable to assume that the absolute value of ε_b is dominated by induced dipoles caused by the ionic and atomic polarizability. As the same ions and atoms exist both in the DWs and in the bulk, ε_i (=ε_{IBLC}) and ε_b (=ε_∞) should be of similar order.

To utilize Equation 1, the next step is to find the total IBLC thickness, d_i, the sum of the thicknesses of all insulating DWs that the current has to cross. This is justified by the fact that a series connection of several identical capacitors is equivalent to a single capacitor with added-up thicknesses of the individual capacitors. Defining d_{DW} as the thickness of a single DW and n_{DW} as the number of insulating DWs per length scale crossed by the current leads to

$$d_i = n_{DW}\, d_b\, d_{DW}, \qquad \text{(Equation 2)}$$

putting Equation 2 into Equation 1 and using $\varepsilon_b = \varepsilon_\infty$, we finally get

$$\varepsilon_{col} = \frac{\varepsilon_\infty}{n_{DW}\, d_{DW}}. \qquad \text{(Equation 3)}$$

Thus, the presence of insulating DWs should lead to an effective enhancement of ε' by a factor $f_{DW} = 1/(n_{DW}\, d_{DW})$. To find n_{DW} for our experimental data, a line was drawn every 5 μm across the SEM image of the sample's domain structure (Figures 1B and 1C), and the number of intersections with DWs along the lines was counted and averaged across all lines. As only some of the DWs are insulating in this system (see Meier et al.[18] for a detailed discussion), the number of insulating DWs is estimated to be half of the total number of intersections. We note that similar assumptions were made in a previous work.[15] The quantity d_{DW} corresponds to the thickness of the "electrically dressed walls," described by Meier et al.[18] as the region in which the local conductance deviates from that of the bulk. Here, we use a value of 150 nm to be consistent with Puntigam et al.[15] We also highlight, as mentioned in Meier et al.,[18] that this value is empirical and depends on multiple factors, including the measurement voltage and the angle of the polar discontinuity.

For the post-annealing state, our fits give $\varepsilon_\infty \approx 21$, and direct measurements of the domain structure as described above lead to $n_{DW}\, d_{DW} \approx 0.0116$ (± 0.0038)

Table 2. A comparison of values from this work with literature

Sample	ε_∞	n_{DW} (1/μm)	n_{DW} d_{DW} (%)	Estimated ε_{col}	Measured ε_{col}	Calculated n_{DW} (1/μm)
h-$ErMnO_3$, pre-annealing	23 (±2)	0.257 (± 0.025)	3.86 (± 0.38)	600 (±80)	–	–
h-$ErMnO_3$, post-annealing	21 (±2)	0.077 (± 0.025)	1.16 (± 0.38)	1,810 (±620)	2,500 (±200)	0.056 (±0.007)
h-$ErMnO_3$[15]	32 (±3)	0.50 (± 0.05)	7.50 (± 0.75)	430 (±60)	250 (±50)	0.85 (±0.19)
h-(Er,Ca)MnO_3[15]	18	0.46	7	260	220	0.54
h-$YMnO_3$ #1[16]	20	0.17	2.5	800	670	0.20

and $f \approx 86$. Using Equation 3, this allows us to derive a colossal static dielectric constant of the IBLC-related MW relaxation of ε_{col} = 1,810 (±620). This is in reasonable agreement with the value found from our fits to the spectra in Figure 3, ε_{col} = 2,500 (±200). While it is not possible to experimentally derive ε_{col} of the invisible IBLC-related MW relaxation for the untreated sample, we can estimate its ε_{col} value using the same formula, which gives ε_{col} = 600 (±80). This smaller value of ε_{col} reflects the larger number of DWs passed by the current in this sample, leading to higher total interface thickness. ε_{col} = 600 is much smaller than the colossal static dielectric constant ascribed to the SBLCs in this sample (about 3×10^4; cf. Figures 3A and Table 1), making it plausible that here, the IBLC relaxation is superimposed by the dominant SBLC relaxation. The smaller expected value ε_{col} = 600 from IBLCs also confirms that the large, single MW relaxation, observed in the pre-annealing state, was correctly assigned to SBLCs.

To highlight the key point that a change in the volume fraction of DWs allows post-synthesis engineering of the dielectric response, we plot the data of Table 2 in Figure 4. The symbols show the measured data points, and the trend line follows Equation 3. From Figure 4 and Equations 1, 2, and 3, it is clear that the ideal structure to get a CDC would be a sample with a single, very thin insulating DW. This is readily explained if the individual walls behave as ideal capacitors added in series so that every additional capacitor reduces the total value. For a single DW, Equations 2 and 3, assuming an increase in the number of DWs for increasing sample thickness, are no longer valid, and we have to revert to the more general Equation 1. It implies that the colossal ε' then can be even further enhanced by using a thicker crystal. Note that the error bars represent the quantifiable errors, while the dominant error is expected to be the extent that surface images of the domain structure can be extrapolated into the bulk of the sample.

DISCUSSION

We have demonstrated the ability to control the dielectric properties of ferroelectrics by adjusting the density of insulating DWs. In the case of $ErMnO_3$, it is correlated with the emergence of characteristic 6-fold meeting points (vertex lines), which can readily be controlled via thermal treatment, providing a viable pathway for adjusting the dielectric response of the system. Our findings show a close, quantitative correlation between the DW density within the same sample and the resulting dielectric constant, which supports previous reports that use different densities of DWs across multiple samples. Consistent with previous studies, we have observed that the insulating DWs behave as ideal capacitors added in series at these voltages. Our findings demonstrate the feasibility of post-synthesis engineering of dielectric responses in materials, with the potential for expansion to other control methods such as electric fields and mechanical stress. This approach offers an additional degree of flexibility and the possibility of dynamic real-time tuning of the dielectric constant, readily applicable to any material with similar robust insulating DWs, such as the isostructural indates, ferrites, or vanadates.[42]

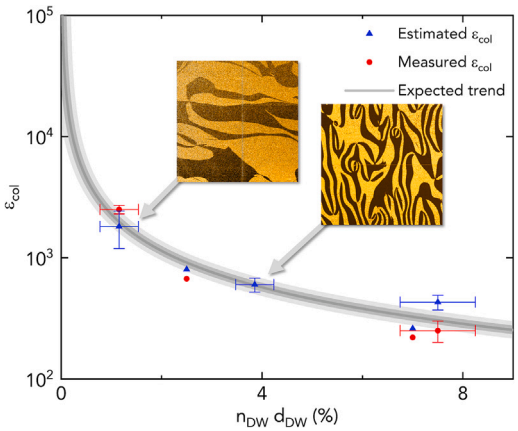

Figure 4. Dependency of ε_{col} on the volume fraction of insulating domain walls

The data points are taken from Table 2, and the gray line is a guide for the eyes, based on the estimated trend predicted by Equation 3, assuming ε_∞ = 22.8. Insets show the respective polar domain structures from Figure 1. The error bars represent the known quantifiable errors, where avalible.

EXPERIMENTAL PROCEDURES

Resource availability

Lead contact

Further information and requests for resources should be directed to the lead contact, Donald M. Evans (donald.evans@warwick.ac.uk).

Materials availability

This study did not generate unique materials.

Data and code availability

The data that support the findings of this study are available from the corresponding author upon reasonable request.

Characterization

For the pre-annealing measurements, the sample had an area of 2.18 mm^2 and a thickness of 1.74 mm. During annealing, some of the sample broke off, so the sample had an area of 1.72 mm^2 and a thickness of 1.72 mm for the post-annealing measurements.

The dielectric data were collected with an Alpha-A high-performance frequency analyzer from Novocontrol Technologies (frequency range: 3 μHz–10 MHz) applying an AC voltage of 1 V. The recorded data are conductance, G', and the real part of the complex capacitance, C'. In the pre-annealing state, the measurements were conducted in a Janis research SHI-950 refrigerator system cold head cryostat, and the post-annealing state was measured in a closed cycle refrigerator (Cryodyne Refrigeration System Model 22 from CTI-Cryogenics). For both measurements, the sample was prepared in a parallel-plate capacitor geometry with top and bottom electrodes made from silver paste (Leitsilber 200N Hans Wolbring).

The SEM images were collected with a ZEISS Crossbeam 550 with ZEISS Gemini 2 electron optics, using the in-lens detector, with an electron beam of 500 pA and 5 kV (Figure 1B) and 200 pA and 5 kV (Figure 1C). The PFM experiments were carried out on a Bruker Dimension Icon AFM using n-doped silicon tips coated with Pt-Ir (SCM-PIT-V2, Bruker). The PFM was collected with an amplitude of 10 V and resonance frequencies of 71.01 and 69.47 kHz, as shown in Figures 1B and 1C, respectively.

ACKNOWLEDGMENTS

The authors thank Dr. Markus Altthaler for his skill and experience in the collection of the SEM images. Crystals were grown at the Lawrence Berkeley Laboratory

supported by the US Department of Energy, Office of Science, Basic Energy Sciences, Materials Sciences and Engineering Division (contract no. DE-AC02-05-CH11231). L.P., P.L., and S.K. acknowledge the financial support of Deutsche Forschungsgemeinschaft Sachbeihilfe (DFG) via the Transregional Research Collaboration TRR 80 (Augsburg, Munich, and Stuttgart; project no. 107745057). D.M.E. wishes to acknowledge and thank the DFG for financial support via DFG individual fellowship number EV 305/1-1 and also acknowledge funding from the Engineering and Physical Sciences Research Council (EP/T027207/1). J.S. acknowledges support from the Alexander von Humboldt Foundation through the Feodor-Lynen fellowship. D.M. thanks NTNU for support through the Onsager Fellowship Program and the Outstanding Academic Fellow Program and acknowledges funding from the European Research Council (ERC) under the European Union's Horizon 2020 Research and Innovation Programme (grant agreement no. 863691).

AUTHOR CONTRIBUTIONS

Conceptualization, S.K. and D.M.E.; methodology, P.L., D.M., S.K., and D.M.E.; validation, S.K. and D.M.E.; formal analysis, L.Z., P.L., S.K., and D.M.E.; investigation, L.Z. and L.P.; writing – original draft, S.K. and D.M.E.; writing – review & editing, L.Z., L.P., P.L., I.K., D.M., S.K., and J.S.; resources, E.B., Z.Y., D.M., and I.K.; visualization, L.Z. and D.M.E.; supervision, S.K. and D.M.E.

DECLARATION OF INTERESTS

The authors declare no competing interests.

DECLARATION OF GENERATIVE AI AND AI-ASSISTED TECHNOLOGIES IN THE WRITING PROCESS

During the preparation of this work, the author(s) used ChatGPT in order to offset issues arising from the corresponding author's dyslexia. After using this tool/service, the author(s) reviewed and edited the content as needed and take(s) full responsibility for the content of the publication.

Received: January 25, 2024
Revised: March 26, 2024
Accepted: April 16, 2024
Published: May 9, 2024

REFERENCES

1. Kishi, H., Mizuno, Y., and Chazono, H. (2003). Base-Metal Electrode-Multilayer Ceramic Capacitors: Past, Present and Future Perspectives. Jpn. J. Appl. Phys. *42*, 1–15. https://doi.org/10.1143/jjap.42.1.

2. Hong, K., Lee, T.H., Suh, J.M., Yoon, S.-H., and Jang, H.W. (2019). Perspectives and challenges in multilayer ceramic capacitors for next generation electronics. J. Mater. Chem. C *7*, 9782–9802. https://doi.org/10.1039/c9tc02921d.

3. Li, J., Shen, Z., Chen, X., Yang, S., Zhou, W., Wang, M., Wang, L., Kou, Q., Liu, Y., Li, Q., et al. (2020). Grain-orientation-engineered multilayer ceramic capacitors for energy storage applications. Nat. Mater. *19*, 999–1005. https://doi.org/10.1038/s41563-020-0704-x.

4. Pan, M.-J., and Randall, C.A. (2010). A brief introduction to ceramic capacitors. IEEE Electr. Insul. Mag. *26*, 44–50. https://doi.org/10.1109/mei.2010.5482787.

5. Lunkenheimer, P., Krohns, S., Riegg, S., Ebbinghaus, S.G., Reller, A., and Loidl, A. (2010). Colossal dielectric constants in transition-metal oxides. Eur. Phys. J. Spec. Top. *180*, 61–89. https://doi.org/10.1140/epjst/e2010-01212-5.

6. Lunkenheimer, P., Bobnar, V., Pronin, A.V., Ritus, A.I., Volkov, A.A., and Loidl, A. (2002). Origin of apparent colossal dielectric constants. Phys. Rev. B *66*, 052105. https://doi.org/10.1103/physrevb.66.052105.

7. Ihlefeld, J.F., Harris, D.T., Keech, R., Jones, J.L., Maria, J., and Trolier-McKinstry, S. (2016). Scaling Effects in Perovskite Ferroelectrics: Fundamental Limits and Process-Structure-Property Relations. J. Am. Ceram. Soc. *99*, 2537–2557. https://doi.org/10.1111/jace.14387.

8. Sinclair, D.C., Adams, T.B., Morrison, F.D., and West, A.R. (2002). $CaCu_3Ti_4O_{12}$: One-step internal barrier layer capacitor. Appl. Phys. Lett. *80*, 2153–2155. https://doi.org/10.1063/1.1463211.

9. Shirane, G., and Takeda, A. (1952). Phase Transitions in Solid Solutions of $PbZrO_3$ and $PbTiO_3$ (I) Small Concentrations of $PbTiO_3$. J. Phys. Soc. Jpn. *7*, 5–11. https://doi.org/10.1143/jpsj.7.5.

10. Adams, T.B., Sinclair, D.C., and West, A.R. (2002). Giant Barrier Layer Capacitance Effects in $CaCu_3Ti_4O_{12}$ Ceramics. Adv. Mater. *14*, 1321–1323. https://doi.org/10.1002/1521-4095(20020916)14:18<1321::aid-adma1321>3.0.co;2.

11. Frey, M.H., Xu, Z., Han, P., and Payne, D.A. (1998). The role of interfaces on an apparent grain size effect on the dielectric properties for ferroelectric barium titanate ceramics. Ferroelectrics *206*, 337–353. https://doi.org/10.1080/00150199808009168.

12. Zhao, Z., Buscaglia, V., Viviani, M., Buscaglia, M.T., Mitoseriu, L., Testino, A., Nygren, M., Johnsson, M., and Nanni, P. (2004). Grain-size effects on the ferroelectric behavior of dense nanocrystalline $BaTiO_3$ ceramics. Phys. Rev. B *70*, 024107. https://doi.org/10.1103/physrevb.70.024107.

13. Krohns, S., Lunkenheimer, P., Ebbinghaus, S.G., and Loidl, A. (2007). Broadband dielectric spectroscopy on single-crystalline and ceramic $CaCu_3Ti_4O_{12}$. Appl. Phys. Lett. *91*, 022910. https://doi.org/10.1063/1.2757098.

14. Krohns, S., Lunkenheimer, P., Kant, C., Pronin, A.V., Brom, H.B., Nugroho, A.A., Diantoro, M., and Loidl, A. (2009). Colossal dielectric constant up to gigahertz at room temperature. Appl. Phys. Lett. *94*, 122903. https://doi.org/10.1063/1.3105993.

15. Puntigam, L., Schultheiß, J., Strinic, A., Yan, Z., Bourret, E., Altthaler, M., Kézsmárki, I., Evans, D.M., Meier, D., and Krohns, S. (2021). Insulating improper ferroelectric domain walls as robust barrier layer capacitors. J. Appl. Phys. *129*, 084101. https://doi.org/10.1063/5.0038300.

16. Ruff, E., Krohns, S., Lilienblum, M., Meier, D., Fiebig, M., Lunkenheimer, P., and Loidl, A. (2017). Conductivity Contrast and Tunneling Charge Transport in the Vortexlike Ferroelectric Domain Patterns of Multiferroic Hexagonal $YMnO_3$. Phys. Rev. Lett. *118*, 036803. https://doi.org/10.1103/physrevlett.118.036803.

17. Schultheiß, J., Picht, G., Wang, J., Genenko, Y.A., Chen, L.Q., Daniels, J.E., and Koruza, J. (2023). Ferroelectric polycrystals: Structural and microstructural levers for property-engineering via domain-wall dynamics. Prog. Mater. Sci. *136*, 101101. https://doi.org/10.1016/j.pmatsci.2023.101101.

18. Meier, D., Seidel, J., Cano, A., Delaney, K., Kumagai, Y., Mostovoy, M., Spaldin, N.A., Ramesh, R., and Fiebig, M. (2012). Anisotropic conductance at improper ferroelectric domain walls. Nat. Mater. *11*, 284–288. https://doi.org/10.1038/nmat3249.

19. Evans, D.M., Garcia, V., Meier, D., and Bibes, M. (2020). Domains and domain walls in multiferroics. Phys. Sci. Rev. *5*, 20190067. https://doi.org/10.1515/psr-2019-0067.

20. Levanyuk, A.P., and Sannikov, D.G. (1974). Improper ferroelectrics. Sov. Phys. Usp. *17*, 199–214. https://doi.org/10.1070/pu1974v017n02abeh004336.

21. Dvořák, V. (1974). Improper ferroelectrics. Ferroelectrics *7*, 1–9. https://doi.org/10.1080/00150197408237942.

22. Lilienblum, M., Lottermoser, T., Manz, S., Selbach, S.M., Cano, A., and Fiebig, M. (2015). Ferroelectricity in the multiferroic hexagonal manganites. Nat. Phys. *11*, 1070–1073. https://doi.org/10.1038/nphys3468.

23. Choi, T., Horibe, Y., Yi, H.T., Choi, Y.J., Wu, W., and Cheong, S.-W. (2010). Insulating interlocked ferroelectric and structural antiphase domain walls in multiferroic $YMnO_3$. Nat. Mater. *9*, 253–258. https://doi.org/10.1038/nmat2632.

24. Wu, W., Horibe, Y., Lee, N., Cheong, S.-W., and Guest, J.R. (2012). Conduction of Topologically Protected Charged Ferroelectric Domain Walls. Phys. Rev. Lett. *108*, 077203. https://doi.org/10.1103/physrevlett.108.077203.

25. Van Aken, B.B., Palstra, T.T.M., Filippetti, A., and Spaldin, N.A. (2004). The origin of ferroelectricity in magnetoelectric $YMnO_3$. Nat. Mater. *3*, 164–170. https://doi.org/10.1038/nmat1080.

26. Smolenskii, G.A., and Bokov, V.A. (1964). Coexistence of Magnetic and Electric Ordering in Crystals. J. Appl. Phys. *35*, 915–918. https://doi.org/10.1063/1.1713535.

27. Yan, Z., Meier, D., Schaab, J., Ramesh, R., Samulon, E., and Bourret, E. (2015). Growth of high-quality hexagonal $ErMnO_3$ single crystals by the pressurized floating-zone method. J. Cryst. Growth *409*, 75–79. https://doi.org/10.1016/j.jcrysgro.2014.10.006.

28. šafránková, M., Fousek, J., and KiŽaev, S.A. (1967). Domains in ferroelectric $YMnO_3$. Czech. J. Phys. *17*, 559–560. https://doi.org/10.1007/bf01695179.

29. Holtz, M.E., Shapovalov, K., Mundy, J.A., Chang, C.S., Yan, Z., Bourret, E., Muller, D.A., Meier, D., and Cano, A. (2017). Topological Defects in Hexagonal Manganites: Inner Structure and Emergent Electrostatics. Nano Lett. *17*, 5883–5890. https://doi.org/10.1021/acs.nanolett.7b01288.

30. Roede, E.D., Mosberg, A.B., Evans, D.M., Bourret, E., Yan, Z., van Helvoort, A.T.J., and Meier, D. (2021). Contact-free reversible switching of improper ferroelectric domains by electron and ion irradiation. Apl. Mater. *9*, 021105. https://doi.org/10.1063/5.0038909.

31. Hunnestad, K.A., Roede, E.D., van Helvoort, A.T.J., and Meier, D. (2020). Characterization of ferroelectric domain walls by scanning electron microscopy. J. Appl. Phys. *128*, 191102. https://doi.org/10.1063/5.0029284.

32. Meier, Q., Lilienblum, M., Griffin, S., Conder, K., Pomjakushina, E., Yan, Z., Bourret, E., Meier, D., Lichtenberg, F., Salje, E., et al. (2017). Global Formation of Topological Defects in the Multiferroic Hexagonal Manganites. Phys. Rev. X *7*, 041014. https://doi.org/10.1103/physrevx.7.041014.

33. Griffin, S.M., Lilienblum, M., Delaney, K.T., Kumagai, Y., Fiebig, M., and Spaldin, N.A. (2012). Scaling Behavior and Beyond Equilibrium in the Hexagonal Manganites. Phys. Rev. X *2*, 041022. https://doi.org/10.1103/physrevx.2.041022.

34. Jonscher, A.K. (1977). The 'universal' dielectric response. Nature *267*, 673–679. https://doi.org/10.1038/267673a0.

35. Elliott, S.R. (1987). A.c. conduction in amorphous chalcogenide and pnictide semiconductors. Adv. Phys. *36*, 135–217. https://doi.org/10.1080/00018738700101971.

36. Holstad, T.S., Evans, D.M., Ruff, A., Småbråten, D.R., Schaab, J., Tzschaschel, C., Yan, Z., Bourret, E., Selbach, S.M., Krohns, S., and Meier, D. (2018). Electronic bulk and domain wall properties in B-site doped hexagonal $ErMnO_3$. Phys. Rev. B *97*, 085143. https://doi.org/10.1103/physrevb.97.085143.

37. Evans, D.M., Holstad, T.S., Mosberg, A.B., Småbråten, D.R., Vullum, P.E., Dadlani, A.L., Shapovalov, K., Yan, Z., Bourret, E., Gao, D., et al. (2020). Publisher Correction: Conductivity control via minimally invasive anti-Frenkel defects in a functional oxide. Nat. Mater. *19*, 1254. https://doi.org/10.1038/s41563-020-00823-1.

38. Evans, D.M., Småbråten, D.R., Holstad, T.S., Vullum, P.E., Mosberg, A.B., Yan, Z., Bourret, E., van Helvoort, A.T.J., Selbach, S.M., and Meier, D. (2021). Observation of Electric-Field-Induced Structural Dislocations in a Ferroelectric Oxide. Nano Lett. *21*, 3386–3392. https://doi.org/10.1021/acs.nanolett.0c04816.

39. Ren, P., Fan, H., and Wang, X. (2013). Bulk conduction and nonlinear behaviour in multiferroic $YMnO_3$. Appl. Phys. Lett. *103*, 152905. https://doi.org/10.1063/1.4824916.

40. Skjærvø, S.H., Wefring, E.T., Nesdal, S.K., Gaukås, N.H., Olsen, G.H., Glaum, J., Tybell, T., and Selbach, S.M. (2016). Interstitial oxygen as a source of p-type conductivity in hexagonal manganites. Nat. Commun. *7*, 13745. https://doi.org/10.1038/ncomms13745.

41. Lunkenheimer, P., Fichtl, R., Ebbinghaus, S.G., and Loidl, A. (2004). Nonintrinsic origin of the colossal dielectric constants in $CaCu_3Ti_4O_{12}$. Phys. Rev. B *70*, 172102. https://doi.org/10.1103/physrevb.70.172102.

42. Småbråten, D.R., Meier, Q.N., Skjærvø, S.H., Inzani, K., Meier, D., and Selbach, S.M. (2018). Charged domain walls in improper ferroelectric hexagonal manganites and gallates. Phys. Rev. Materials *2*, 114405. https://doi.org/10.1103/physrevmaterials.2.114405.